

Low-dimensional magnetism of BaCuTe₂O₆

P. Bag,¹ N. Ahmed,¹ Vikram Singh,¹ M. Sahoo,² A. A. Tsirlin,^{3,*} and R. Nath^{1,†}

¹*School of Physics, Indian Institute of Science Education and Research Thiruvananthapuram-695551, India*

²*Department of Physics, University of Kerala, Kariavattom, Thiruvananthapuram-695581, India*

³*Experimental Physics VI, Center for Electronic Correlations and Magnetism, Institute of Physics, University of Augsburg, 86135 Augsburg, Germany*

(Dated: April 1, 2021)

X-ray diffraction, thermodynamic measurements, and density-functional band-structure calculations are used to study the magnetic behavior of BaCuTe₂O₆, a member of the ACuTe₂O₆ structural family that hosts complex three-dimensional frustrated spin networks with possible spin-liquid physics. Temperature-dependent magnetic susceptibility and heat capacity of the Ba compound are well described by the one-dimensional spin- $\frac{1}{2}$ Heisenberg chain model reminiscent of the Sr analog SrCuTe₂O₆. While the intrachain coupling $J/k_B \simeq 37$ K is reduced compared to 49 K in the Sr compound, the Néel temperature increases from 5.5 K (Sr) to 6.1 K (Ba). Unlike the Sr compound, BaCuTe₂O₆ undergoes only one magnetic transition as a function of temperature and shows signatures of weak spin canting. We elucidate the microscopic difference between the Sr and Ba compounds and suggest that one of the interchain couplings changes sign as a result of negative pressure caused by the Sr/Ba substitution. The Néel temperature of BaCuTe₂O₆ is remarkably insensitive to the magnetic dilution with Zn²⁺ up to the highest reachable level of about 20%.

I. INTRODUCTION

Frustrated magnetic networks host unusual ground states and non-trivial dynamical phenomena that become intricate especially in the case of quantum spins [1–3]. Compounds based on the spin- $\frac{1}{2}$ Cu²⁺ ions offer one of the best playgrounds for the experimental realization of such networks. Different types of crystal structures give access to multiple interaction geometries, including kagome lattices of interacting spins [4, 5]. Layered kagome compounds can even be found in nature as copper minerals [6], but their three-dimensional analogs – material realizations of the hyperkagome spin lattice – remain scarce. The only example in the cuprate family is PbCuTe₂O₆ [7, 8], where signatures of a three-dimensional quantum spin liquid with fractional spinon excitations were recently reported [9].

PbCuTe₂O₆ has a fairly complex cubic crystal structure. The hyperkagome lattice formed by second-neighbor interactions is augmented by interactions between first and third neighbors [9]. When Sr substitutes for Pb, the crystal structure and even the cubic lattice parameter remain nearly unchanged, but the magnetic behavior is modified drastically. SrCuTe₂O₆ is a spin-chain compound with a robust magnetic order at low temperatures [10–12]. Predominant third-neighbor interactions give rise to spin chains along each of the three main cubic directions [10]. The presence of multiple phase transitions [10, 13], complex temperature-field phase diagram [12], and non-collinear magnetic order [11, 12] witness frustrated interchain interactions that may be residues of the strong frustration present in PbCuTe₂O₆.

The drastically different behavior of the Pb and Sr compounds suggests an extreme sensitivity of this structure type to chemical substitutions. This fact motivated us to prepare and explore BaCuTe₂O₆, another member of the same family, **and attempt its further tuning by Zn doping that may introduce both chemical pressure and magnetic dilution.**

BaCuTe₂O₆ retains the cubic crystal symmetry and overall structural geometry of the ACuTe₂O₆ compounds, but shows a notable lattice expansion, with the room-temperature cubic lattice parameter increasing from $a = 12.473$ Å [14] (Sr) and $a = 12.49$ Å [7] (Pb) to $a = 12.87$ Å (Ba). We demonstrate that, despite this effective negative pressure, BaCuTe₂O₆ strongly resembles SrCuTe₂O₆ and hosts weakly coupled spin chains due to predominant magnetic interactions between third neighbors. Interestingly, substituting Ba for Sr decreases the intrachain coupling but increases the Néel temperature. We combine this observation with an *ab initio* microscopic analysis to identify relevant magnetic interactions and their changes upon chemical substitutions. **We also show a remarkable insensitivity of the Néel temperature to magnetic dilution as another experimental witness of the underlying frustration in this family of compounds.**

II. METHODS

Polycrystalline samples of Ba(Cu_{1-x}Zn_x)Te₂O₆ ($x = 0 - 0.20$) were synthesized following the same procedure adopted for the synthesis of SrCuTe₂O₆ [10]. The initial reactants BaCO₃ (Aldrich, 99.995%), CuO (Aldrich, 99.999%), TeO₂ (Aldrich, 99.995%), H₂TeO₄·2H₂O (Alfa Aesar, 99%), and ZnO (Aldrich, 99.99%) were taken in stoichiometric ratios required for the synthesis of BaCuTe₂O₇ and its Zn doped samples. For $x = 0$, the reactants were ground thoroughly, pelletized, and fired

* altsirlin@gmail.com

† rnath@iisertvm.ac.in

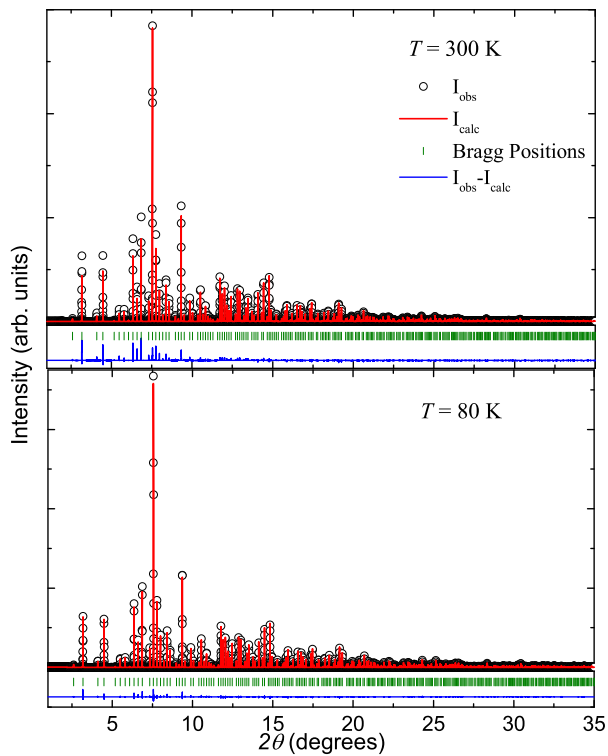


FIG. 1. Synchrotron x-ray diffraction data of $\text{BaCuTe}_2\text{O}_6$ at 300 K and 80 K. The solid lines denote the Rietveld fits of the data. The Bragg peak positions are indicated by green vertical bars, and the bottom blue line shows the difference between the experimental and calculated intensities. **The refinement residuals R_I/R_p are 0.028/0.092 at 300 K and 0.016/0.076 at 80 K.**

at 670 °C for five days in flowing argon atmosphere with several intermediate grindings. For the doped samples, the firing temperature was varied from 670 °C to 720 °C.

Similar to $\text{SrCuTe}_2\text{O}_6$, the flowing argon provides a reducing atmosphere which leads to the loss of oxygen and hence the formation of $\text{BaCuTe}_2\text{O}_6$ instead of $\text{BaCuTe}_2\text{O}_7$. The powder x-ray diffraction (XRD) pattern was recorded at room temperature using a PANalytical powder diffractometer ($\text{CuK}\alpha$ radiation, $\lambda_{\text{avg}} \simeq 1.5418 \text{ \AA}$). **The samples were found to be single-phase up to $x = 0.18$, while for $x = 0.20$ $\text{BaCuTe}_2\text{O}_7$ emerged as a minor impurity phase.** The amount of the impurity phase for $x = 0.20$ was found to be very small (about $\sim 2\%$). Our repeated attempts to achieve higher doping levels by increasing or lowering the firing temperature were unsuccessful.

For structure determination, high-resolution synchrotron XRD data were collected at the ID22 beamline of ESRF using the wavelength of 0.4107 Å. The powder sample placed into a thin-wall borosilicate capillary was cooled down with liquid-nitrogen cryostream and spun during the measurement. Diffracted signal was measured by 9 scintillation detectors, each preceded by a Si (111) analyzer crystal. Rietveld refinements of the XRD data

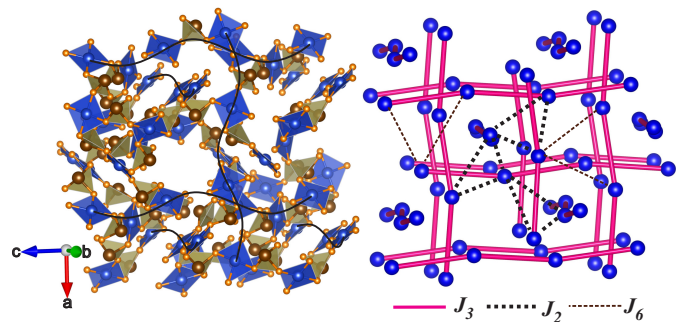


FIG. 2. Left panel: Crystal structure of $\text{BaCuTe}_2\text{O}_6$, with black curved lines denoting the spin chains. The blue square planes are the CuO_4 plaquettes, while the TeO_3 units are shown in green color. The Ba atoms are omitted for clarity. Right panel: spin lattice of $\text{BaCuTe}_2\text{O}_6$ composed of crossed spin chains (solid red lines) of Cu^{2+} ions. The dominant interchain couplings J_2 and J_6 forming frustrated loops are also shown. VESTA software was used for crystal structure visualization [15].

were performed using JANA2006 and FULLPROF software packages [16, 17].

Magnetic susceptibility χ ($\equiv M/H$, M is the magnetization and H is the applied field) was measured as a function of temperature ($2 \text{ K} \leq T \leq 350 \text{ K}$) and magnetic field ($0 \text{ T} \leq H \leq 9 \text{ T}$) using a vibrating sample magnetometer (VSM) attachment to the Physical Property Measurement System (PPMS, Quantum Design). Heat capacity C_p was measured on a small piece of the sintered pellet via the relaxation technique using the heat capacity option of PPMS.

Exchange parameters were calculated for the spin Hamiltonian

$$\mathcal{H} = \sum_{\langle ij \rangle} J_{ij} \mathbf{S}_i \mathbf{S}_j, \quad (1)$$

where the summation is over lattice bonds $\langle ij \rangle$. Exchange integrals J_{ij} were extracted via density-functional (DFT) band structure calculations performed using the FPL0 code [18] within generalized gradient approximation (GGA) [19] for the exchange-correlation potential. The mean-field GGA+ U approach was used to treat correlation effects in the Cu 3d shell, with the Hubbard repulsion parameter $U_d = 8.5 \text{ eV}$, Hund's coupling $J_d = 1 \text{ eV}$, and double-counting correction in the atomic limit [20, 21]. All calculations were performed for the crystallographic unit cell with 120 atoms, and reciprocal space was sampled by 64 \mathbf{k} -points in the symmetry-irreducible part of the first Brillouin zone. Experimental structural parameters were used, as further described in Sec. III D.

TABLE I. Atomic positions and isotropic atomic displacement parameters (U_{iso} , in units of 10^{-2} \AA^2) for $\text{BaCuTe}_2\text{O}_6$ at 80 K (upper lines) and 300 K (lower lines) obtained from the refinement of the synchrotron data. The cubic lattice parameter is $a = 12.8296(1) \text{ \AA}$ at 80 K and $a = 12.8699(1) \text{ \AA}$ at 300 K. The space group is $P4_132$. All the sites are fully occupied.

Atom	Wyckoff position	x/a	y/a	z/a	U_{iso}
Ba1	8c	0.05757(3)	0.05757(3)	0.05757(3)	0.35(2)
		0.05825(4)	0.05825(4)	0.05825(4)	1.29(2)
Ba2	4b	0.375	0.625	0.125	0.41(2)
		0.375	0.625	0.125	1.33(3)
Cu	12d	0.47429(7)	0.875	0.27571(7)	0.37(3)
		0.47381(9)	0.875	0.27619(9)	1.17(2)
Te	24e	0.33709(4)	0.91707(4)	0.06354(4)	0.39(1)
		0.33709(4)	0.91657(5)	0.06425(5)	1.31(1)
O1	24e	0.3763(3)	0.8256(3)	0.1734(3)	0.29(1)
		0.3760(4)	0.8254(4)	0.1733(4)	1.01(1)
O2	24e	0.2664(3)	0.8115(3)	-0.0121(3)	0.52(1)
		0.2673(4)	0.8117(4)	-0.0163(4)	1.82(1)
O3	24e	0.2259(3)	0.9751(3)	0.1360(4)	0.89(1)
		0.2265(4)	0.9746(4)	0.1376(4)	2.39(1)

III. RESULTS

A. Crystal Structure

To the best of our knowledge, synthesis and characterization of $\text{BaCuTe}_2\text{O}_6$ have not been reported previously. To establish the crystal structure of this compound, Rietveld refinement of the synchrotron XRD data was performed using the structural data of $\text{SrCuTe}_2\text{O}_6$ as the starting model [14]. Figure 1 presents the synchrotron XRD data at two different temperatures along with the Rietveld fits. The results are listed in Table I and suggest close similarity to the Sr compound. At 80 K, all atomic displacement parameters are reduced with respect to their room-temperature values, indicating the absence of structural disorder. The incorporation of Ba has the effect of negative pressure and increases the Cu-Cu distances compared to $\text{SrCuTe}_2\text{O}_6$ (see also Table II).

Figure 2 shows the crystal structure of $\text{BaCuTe}_2\text{O}_6$. The CuO_4 plaquettes are linked into a 3D network via TeO_3 trigonal pyramids. This geometrical arrangement allows for several interaction topologies, including isolated triangles formed by the nearest-neighbor interaction J_1 , the hyperkagome lattice formed by the second-neighbor interaction J_2 , and crossed spin chains formed by the third-neighbor interaction J_3 (see also Fig. 10). This latter interaction is predominant in $\text{BaCuTe}_2\text{O}_6$, as

we show in the following.

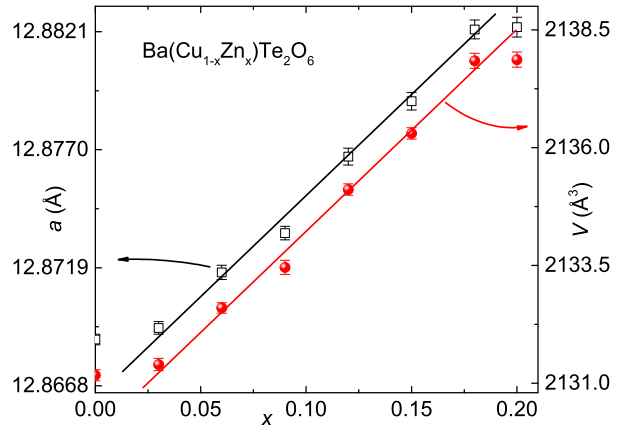


FIG. 3. Variation of lattice constant (a) and unit cell volume (V) with Zn^{2+} concentration (x), obtained from the Rietveld refinement of the powder XRD data at room temperature for $\text{Ba}(\text{Cu}_{1-x}\text{Zn}_x)\text{Te}_2\text{O}_6$. Solid lines are the linear fits as per the Vegard's law.

We have also prepared Zn-doped samples that preserve the cubic symmetry up to the highest doping level of $x \simeq 0.2$. The lattice constant (a) increases almost linearly but weakly with Zn concentration (x) (see Fig. 3). This leads to an overall linear increase in the unit cell volume (V). Though the change is marginal, the increasing trend resembles other Zn-doped Cu^{2+} compounds [22] and complies with the slightly larger ionic radius of Zn^{2+} (0.6 \AA) compared to Cu^{2+} (0.57 \AA).

B. Magnetic Susceptibility

Temperature-dependent magnetic susceptibility $\chi(T)$ measured in an applied magnetic field $\mu_0 H = 1 \text{ T}$ is shown in the upper panel of Fig. 4. It follows a Curie-Weiss (CW) behavior in the high-temperature regime. A broad maximum at $T_{\chi}^{\text{max}} \simeq 20 \text{ K}$ is the signature of short-range order, typically observed in low-dimensional antiferromagnetic (AFM) spin systems. The temperature corresponding to the broad maximum is a measure of the strength of the dominant AFM exchange interaction [23–25]. With decreasing temperature, a sharp peak reminiscent of a transition toward magnetic long-range order (LRO) is observed at $T_N \simeq 6.1 \text{ K}$. When the temperature is lowered further, a small Curie-like upturn in $\chi(T)$ is seen, which is due to the small amount of extrinsic paramagnetic impurities or intrinsic defects present in the sample.

The $\chi(T)$ data in the high-temperature region were fitted by the following expression:

$$\chi(T) = \chi_0 + \frac{C}{T + \theta_{\text{CW}}}. \quad (2)$$

Here χ_0 is the temperature-independent susceptibility that includes contributions of core diamagnetism (χ_{core})

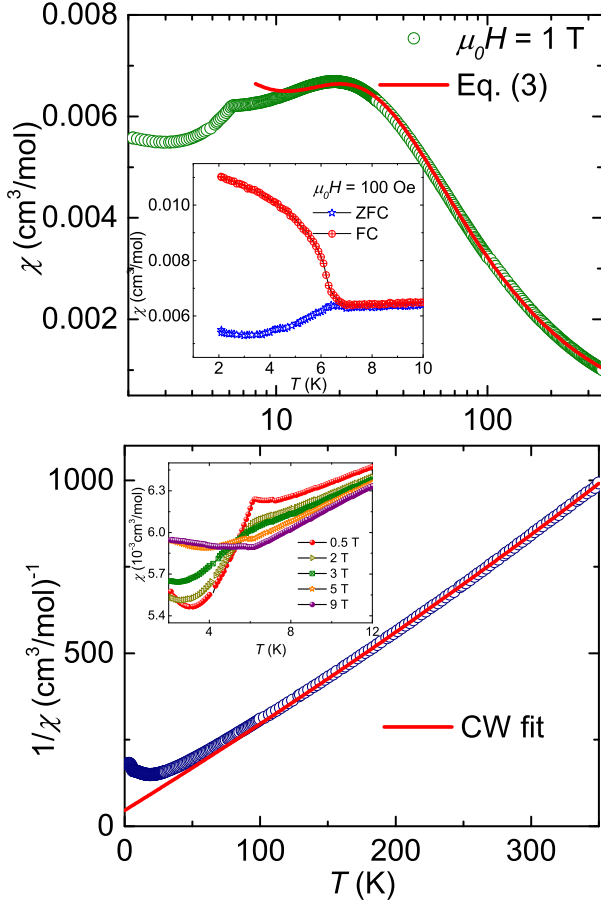


FIG. 4. Upper panel: $\chi(T)$ of $\text{BaCuTe}_2\text{O}_6$ measured in an applied field of $\mu_0 H = 1$ T. The solid red line represents the 1D model fit [Eq. (3)] as described in the text. Inset: ZFC and FC susceptibilities measured at $\mu_0 H = 0.01$ T in the low-temperature regime. Lower panel: Inverse susceptibility $1/\chi$ as a function of temperature. The solid line is the CW fit using Eq. (2). Inset: Low-temperature $\chi(T)$ of $\text{BaCuTe}_2\text{O}_6$ measured at different applied fields up to 9 T.

and Van-Vleck paramagnetism (χ_{VV}). The second term is the CW law with C being the Curie constant and θ_{CW} the characteristic Curie-Weiss temperature. Our fit above 200 K (lower panel of Fig. 4) yields $\chi_0 \simeq -1.19 \times 10^{-4}$ cm³/mol, $C \simeq 0.41$ cm³ K/mol, and $\theta_{\text{CW}} \simeq 18.97$ K. The value of C corresponds to an effective moment $\mu_{\text{eff}} \simeq 1.82 \mu_{\text{B}}$, which is slightly higher than the spin-only value of $\mu_{\text{eff}} = g\sqrt{S(S+1)}\mu_{\text{B}} \simeq 1.73 \mu_{\text{B}}$ for Cu^{2+} ($S = \frac{1}{2}$) and $g = 2$. This is consistent with the g -value slightly above 2.0, as typical for Cu^{2+} compounds [21, 26]. χ_{core} of $\text{BaCuTe}_2\text{O}_6$ was calculated to be -1.43×10^{-4} cm³/mol by adding the χ_{core} of individual ions Ba^{2+} , Cu^{2+} , Te^{4+} , and O^{2-} [27]. χ_{VV} was calculated by subtracting χ_{core} from χ_0 and equals $\sim 2.3 \times 10^{-5}$ cm³/mol. This value of χ_{VV} is comparable to the other cuprate compounds like Sr_2CuO_3 [28], $\text{Sr}_2\text{Cu}(\text{PO}_4)_2$ [29], and $\text{PbCu}_3\text{TeO}_7$ [30]. The value of θ_{CW} is positive and comparable in magnitude to T_{χ}^{max} ,

which implies that the dominant exchange interaction between the Cu^{2+} ions is AFM in nature.

Magnetic susceptibility was further analyzed using the expression

$$\chi(T) = \chi_0 + \frac{C_{\text{imp}}}{T} + \chi_{\text{spin}}(T), \quad (3)$$

where the second term is the Curie law that account for paramagnetic impurities potentially present in the sample, and C_{imp} gauges the impurity concentration. The third term $\chi_{\text{spin}}(T)$ was taken as the expression for the spin susceptibility of a uniform 1D Heisenberg spin- $\frac{1}{2}$ AFM chain given by Johnston *et al* [23]. This expression is valid over a wide temperature range ($5 \times 10^{-25} \leq k_{\text{B}}T/J \leq 5$). The fit above 10 K returned $\chi_0 \simeq -3.76 \times 10^{-5}$ cm³/mol, $C_{\text{imp}} \simeq 0.013$ cm³ K/mol, $g \simeq 2.02$, and $J/k_{\text{B}} \simeq 37.0$ K. From the value of C_{imp} , the impurity concentration is estimated to be $\sim 3\%$, assuming spin- $\frac{1}{2}$ impurities. Below 10 K, experimental susceptibility clearly deviates from the fit. **Our microscopic analysis suggests that interchain interactions do not exceed 5 K (Sec. III D). Therefore, the deviations are most likely caused by anisotropic terms in the spin Hamiltonian, such as Dzyloshinskii-Moriya interaction, which is allowed by symmetry for the intrachain coupling J_3 .**

The Sr compound showed two consecutive transitions as a function of temperature in the magnetic susceptibility and other thermodynamic probes [10, 12, 13]. In contrast, $\text{BaCuTe}_2\text{O}_6$ reveals one transition only (Figs. 4, 5, and 6). Another difference can be seen in very low magnetic fields, where $\text{SrCuTe}_2\text{O}_6$ displayed no significant deviation between the field-cooled (FC) and zero-field cooled (ZFC) $\chi(T)$ measurements [10], while $\text{BaCuTe}_2\text{O}_6$ displays a bifurcation at T_{N} suggestive of a weak spin canting in the magnetically ordered state (see the inset of the upper panel of Fig. 4).

The magnetization isotherm (M vs H) at $T = 2$ K measured upto 9 T is shown in the upper panel of Fig. 5 for both $\text{BaCuTe}_2\text{O}_6$ and $\text{SrCuTe}_2\text{O}_6$. Unlike the Sr compound, the Ba compound exhibits linear behavior without any indications of a field-induced transition. In the inset of Fig. 5, we magnified the data near zero field in order to highlight a tiny remanent magnetization of less than $0.001 \mu_{\text{B}}$ /f.u. present in the Ba compound. This indicates a small spin canting in the antiferromagnetically ordered state.

AC susceptibility as a function of temperature was also measured at different frequencies. The real part of the AC susceptibility (χ') shows a peak at T_{N} , its position not changing with frequency (lower panel of Fig. 5). This excludes freezing effects. We also note that the transition temperature is remarkably insensitive to the applied field (lower panel of Fig. 4).

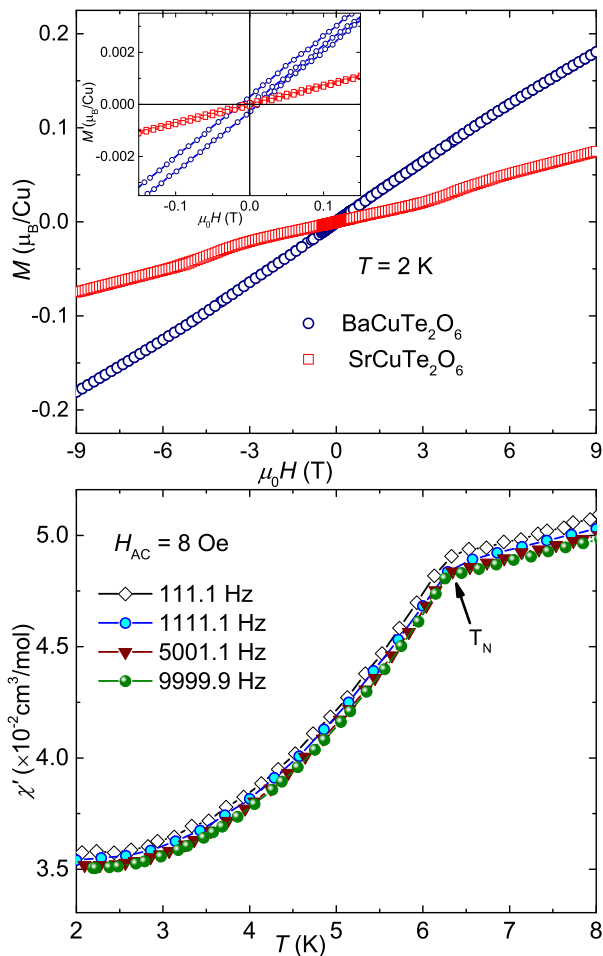


FIG. 5. Upper panel: Magnetic isotherm (M vs H) for $\text{BaCuTe}_2\text{O}_6$ and $\text{SrCuTe}_2\text{O}_6$ at $T = 2$ K. The bend around 3 T in the Sr compound indicates the transition toward a field-induced state [12]. Inset: Magnified M vs H near zero field to highlight the minute net moment present in the Ba compound. Lower panel: Real part of the AC susceptibility (χ') vs T measured on $\text{BaCuTe}_2\text{O}_6$ at different frequencies. The transition temperature is marked by an arrow.

C. Heat Capacity

Heat capacity C_p as a function of temperature measured in zero field is shown in Fig. 6. With decreasing temperature, it decreases rapidly and then shows a sharp λ -type anomaly at $T_N \simeq 6.1$ K, affirming the transition to the magnetically ordered state. In magnetic insulators, C_p has two principal contributions, phononic part and magnetic part that dominate the signal at higher and lower temperatures, respectively.

To estimate the phononic part of the heat capacity (C_{ph}), the raw data at high temperatures were fitted by a linear combination of four Debye functions [31, 32],

$$C_{\text{ph}}(T) = 9R \times \sum_{n=1}^4 c_n \left(\frac{T}{\theta_{\text{Dn}}} \right)^3 \int_0^{\frac{\theta_{\text{Dn}}}{T}} \frac{x^4 e^x}{(e^x - 1)^2} dx. \quad (4)$$

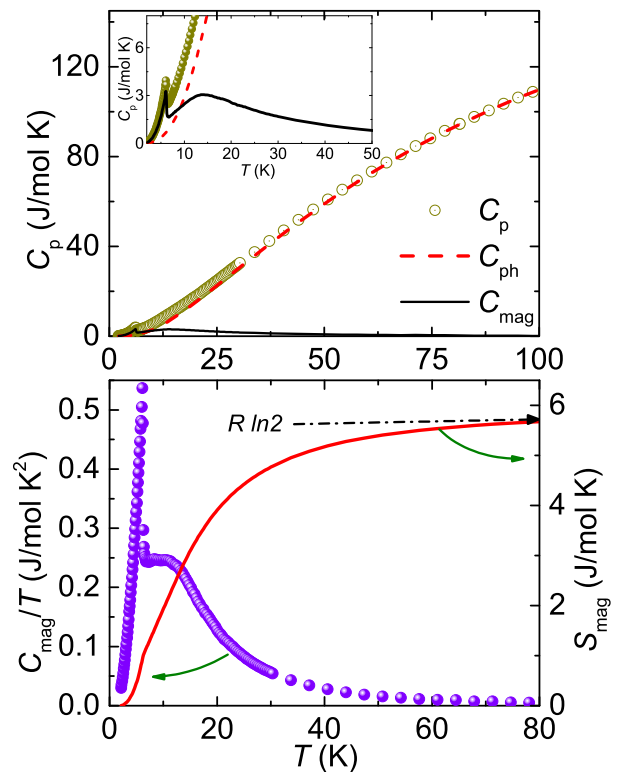


FIG. 6. Upper panel: C_p vs T of $\text{BaCuTe}_2\text{O}_6$ measured in zero applied field. The dashed and solid lines represent the phononic (C_{ph}) fit [Eq. (4)] and magnetic (C_{mag}) parts of $C_p(T)$, respectively. In the inset, $C_{\text{mag}}(T)$ is shown in the magnified form. Lower panel: C_{mag}/T and S_{mag} as a function of T are shown in the left and right y -axes, respectively. The dash-dotted arrow points to the expected value of magnetic entropy $S_{\text{mag}} = R \ln 2$ for Cu^{2+} ($S = \frac{1}{2}$).

Here, $R = 8.314 \text{ J mol}^{-1} \text{ K}^{-1}$ is the universal gas constant. The coefficients c_n represent the groups of distinct atoms in the crystal, and θ_{Dn} are the corresponding Debye temperatures. Since there are four different atoms with largely different atomic mass, we used four ($n = 4$) Debye functions. The solid dashed curve in Fig. 6 (upper panel) represents the Debye fit (C_{ph}) of the $C_p(T)$ data at high temperatures ($T \geq 50$ K) using Eq. (4) and is extrapolated down to low temperatures.

Magnetic part of the heat capacity (C_{mag}) was obtained by subtracting C_{ph} from the total heat capacity C_p . The subtraction procedure was verified by calculating the magnetic entropy S_{mag} through the integration of $C_{\text{mag}}(T)/T$ that yields $S_{\text{mag}} \simeq 5.87 \text{ J mol}^{-1} \text{ K}^{-1}$ at 80 K (lower panel of Fig. 6). This value is close to the expected magnetic entropy for spin- $\frac{1}{2}$: $S_{\text{mag}} = R \ln 2 = 5.76 \text{ J mol}^{-1} \text{ K}^{-1}$. In order to highlight the low-temperature features, we magnified the low-temperature data in the inset of Fig. 6. C_{mag} shows a clear broad maximum at $T_C^{\text{max}} \simeq 13.6$ K representing the short-range AFM correlations similar to that observed in $\chi(T)$. Both shape and magnitude of the maximum compare fa-

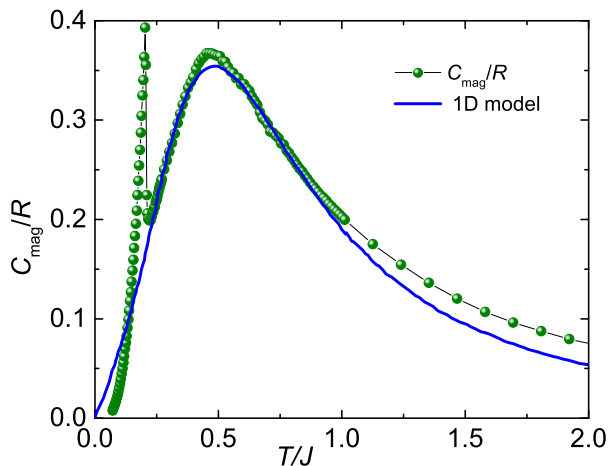


FIG. 7. C_{mag}/R vs T of $\text{BaCuTe}_2\text{O}_6$ in zero magnetic field. The solid line is the series expansion result for the 1D spin- $\frac{1}{2}$ chain model from Ref. [23] with the exchange coupling $J/k_B \simeq 30$ K.

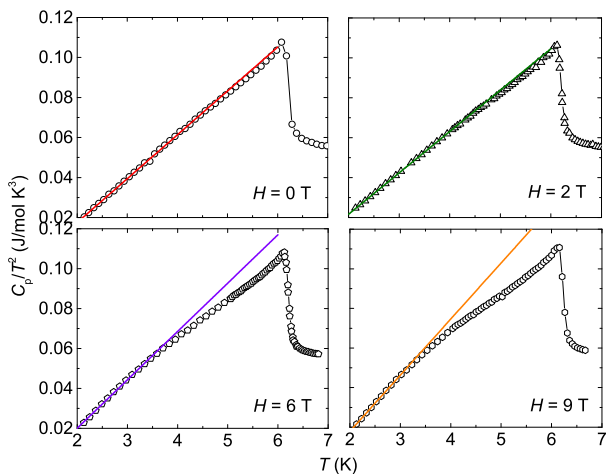


FIG. 8. C_p/T^2 vs T measured under different magnetic fields from 0 to 9 T. Solid line represents the fit by $C_p \propto T^3$ in the low-temperature region, well below T_N .

vorably with theoretical results for the spin-chain model (Fig. 7) [23].

Figure 8 shows C_p/T^2 vs T measured in different applied fields at low temperatures. The value of T_N is found to remain unchanged under external magnetic field up to 9 T similar to that observed in $\chi(T)$. Below T_N , $C_p(T)$ follows a T^3 behaviour at all fields, as expected for a 3D Heisenberg antiferromagnet. This indicates the smallness (or absence) of an anisotropy gap in the spin-wave spectrum.

D. Microscopic magnetic model

We now compare and contrast $\text{BaCuTe}_2\text{O}_6$ with its Sr analog. To this end, magnetic interactions are calcu-

TABLE II. Interatomic distances d_i (in Å), hopping parameters t_i (in meV), and exchange integrals J_i (in K) for $\text{SrCuTe}_2\text{O}_6$ (upper rows) and $\text{BaCuTe}_2\text{O}_6$ (lower rows). The interatomic distances are given according to the experimental crystal structures of both compounds determined at 80 K, only the shortest $\text{O}\cdots\text{O}$ distance is listed. AFM contributions to the exchange couplings are obtained as $J_i^{\text{AFM}} = 4t_i^2/U_{\text{eff}}$ with $U_{\text{eff}} = 4.5$ eV. Total exchange integrals J_i are obtained by a GGA+ U mapping procedure. The interactions beyond J_6 are negligible.

	$d_{\text{Cu-Cu}}$	$d_{\text{O}\cdots\text{O}}$	t_i	J_i^{AFM}	J_i	
J_1	4.530	3.262	10	1	0	Sr
	4.736	3.412	10	1	0	Ba
J_2	5.511	2.747	25	7	-5	Sr
	5.656	2.772	46	22	5	Ba
J_3	6.276	2.773	-87	78	47	Sr
	6.482	2.927	-73	55	34	Ba
J_4	7.453	-	0	0	0	Sr
	7.704	-	-2	0	0	Ba
J_5	8.740	-	0	0	0	Sr
	9.034	-	0	0	0	Ba
J_6	8.949	-	-20	4	2	Sr
	9.196	-	-18	4	2	Ba

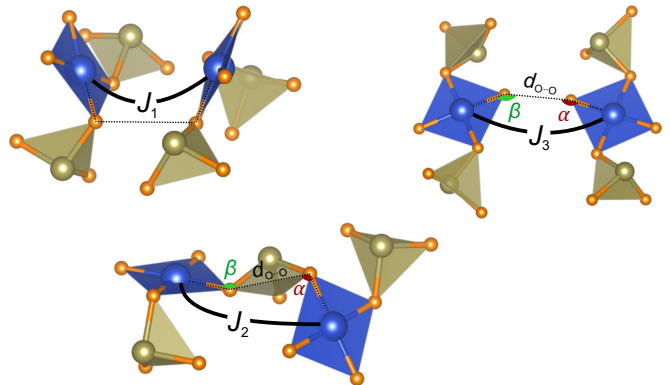


FIG. 9. Superexchange pathways for the interactions $J_1 - J_3$. The Cu-O-O angles α and β control the relative strengths of J_2 and J_3 . The $\text{O}\cdots\text{O}$ distances are given in Table II.

lated for the experimental crystal structures of both compounds determined under exactly the same conditions, by refining synchrotron XRD data collected at 80 K (the structural parameters for $\text{SrCuTe}_2\text{O}_6$ are given in the Appendix). This allows us to trace relevant trends even for weak interchain couplings [33].

Exchange parameters J_{ij} of Eq. (1) are obtained via two complementary procedures. First, the uncorrelated GGA band structure is mapped onto a tight-binding model and supplied with an effective Coulomb repulsion $U_{\text{eff}} = 4.5$ eV [26, 34] that yields AFM exchange terms as $J_i^{\text{AFM}} = 4t_i^2/U_{\text{eff}}$, where t_i are the hopping parameters. This way, all relevant exchange couplings, including those

between distant Cu atoms, can be assessed simultaneously. Alternatively, total exchange couplings, including also ferromagnetic terms, were extracted from GGA+ U total energies by a mapping procedure [35, 36].

The results of both methods are listed in Table II. They suggest that both compounds are dominated by the third-neighbor interactions J_3 responsible for the formation of spin chains. The magnitude of J_3 decreases upon replacing Sr with Ba. Microscopically, the coupling J_3 originates from the Cu–O \cdots O–Cu superexchange controlled by the O \cdots O distance (Fig. 9). Such couplings usually occur through the O–O edge of a rigid polyanionic group, which is rather insensitive to pressure effects or chemical substitutions [37]. However, in $ACuTe_2O_6$ the O \cdots O contact of J_3 does not form the edge of the TeO_3 pyramid, so the relevant distance can be quite flexible and increases by about 0.15 Å upon replacing Sr with Ba, thus reducing J_3 (Table II).

The interchain couplings J_1 and J_2 follow a similar superexchange mechanism, but with a largely different interaction geometry (Fig. 9). While J_1 is negligible in both compounds, we find a notable increase in J_2^{AFM} and, correspondingly, a change of sign of J_2 from FM to AFM upon replacing Sr with Ba. Here, the O \cdots O distance is constrained by the edge of the TeO_3 pyramid and changes only weakly, but the linearity of the pathway gauged by the Cu–O–O angles α and β increases: compare $\alpha_{\text{Sr}} = 100.6^\circ$ and $\beta_{\text{Sr}} = 155.2^\circ$ to $\alpha_{\text{Ba}} = 106.1^\circ$ and $\beta_{\text{Ba}} = 159.9^\circ$. In the case of J_3 , $\alpha_{\text{Sr}} = \beta_{\text{Sr}} = 154.5^\circ$ and $\alpha_{\text{Ba}} = \beta_{\text{Ba}} = 153.7^\circ$ give rise to much more “straight” superexchange pathways and cause a much stronger AFM superexchange than J_2 , despite the longer O \cdots O separation. This structural difference elucidates the $J_3 \gg |J_2|$ regime observed in both Sr and Ba compounds.

Similar arguments can be invoked to explain the absence of J_1 , where the O \cdots O distance exceeds 3.2 Å (Table II), while both α and β are in the range of 100–110° and lead to a strong deviation of the pathway from linearity. Such interaction geometry is prohibitive for the superexchange (Fig. 9), similar, for example, to fedotovite and other Cu^{2+} minerals with hexamer clusters [38]. On the other hand, the long-range interaction J_6 appears to be non-negligible and comparable in size in both Sr and Ba compounds (Table II).

We infer that $SrCuTe_2O_6$ and $BaCuTe_2O_6$ should host similar spin lattices where J_1 is nearly absent, whereas J_2 changes sign from FM for $A = Sr$ to AFM for $A = Ba$. This scenario sheds new light on the magnetic structure that has been determined for $SrCuTe_2O_6$ recently. The neutron diffraction studies of Refs. [11, 12] revealed that the spins are antiparallel along the chains, but adopt different directions in different chains. Altogether, six sublattices with different spin directions are formed. The spin direction changes not only between every two orthogonal chains, but also between the two adjacent chains that are parallel to each other [Fig. 10(c)].

In $SrCuTe_2O_6$, this strongly non-collinear spin arrangement gives rise to the coplanar 120° magnetic order

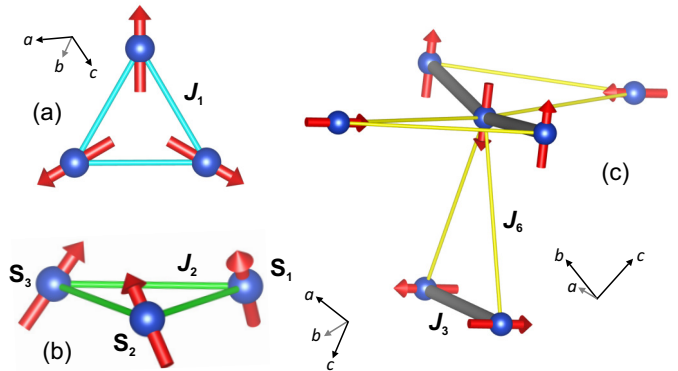


FIG. 10. Frustrated loops formed by the interchain interactions J_1 , J_2 , and J_6 . Experimental magnetic structure of $SrCuTe_2O_6$ [12] is superimposed. We expect that $BaCuTe_2O_6$ has a different spin arrangement according to the different sign of J_2 predicted in our work.

on the triangles formed by J_1 , and the non-coplanar order on the triangles formed by J_2 [Fig. 10(a),(b)]. At first glance, it would indicate that AFM J_1 should be the leading interchain coupling, whereas J_2 is negligible, because any sizable J_2 would cause a different type of order on the J_2 -triangles: collinear ferromagnetic at $J_2 < 0$ and coplanar 120° at $J_2 > 0$. Interestingly, we find a sizable J_2 and neither microscopic indications nor plausible structural reasons for J_1 being the leading interchain coupling in any of the compounds. On the other hand, J_6 is a plausible reason for non-collinearity. This coupling connects a spin of one chain to two adjacent spins in the parallel chain (Fig. 10c). The resulting frustration is alleviated by arranging the spins of these chains along two orthogonal directions, similar to the non-collinear magnetic order in Cu_2GeO_4 [39].

The frustrated nature of J_6 prevents the spins on the J_2 triangles from being parallel, as FM J_2 would require. However, partial FM correlations still occur, with the classical interaction energy,

$$E_2 = J_2(\mathbf{S}_1\mathbf{S}_2 + \mathbf{S}_2\mathbf{S}_3 + \mathbf{S}_1\mathbf{S}_3) = \frac{3}{2}J_2S^2 \quad (5)$$

that allows a sizable energy gain from FM J_2 . This energy gain is in fact equal to the energy gain expected from the 120° order on the J_1 triangle, should the interaction J_1 be AFM in nature. Therefore, AFM J_1 and FM J_2 are equally instrumental in stabilizing the non-collinear magnetic order in $SrCuTe_2O_6$.

A somewhat similar magnetic structure can be envisaged in $BaCuTe_2O_6$. Indeed, changing the spin directions on a given J_2 triangle from

$$\mathbf{S}_1 \parallel [1\bar{1}0], \quad \mathbf{S}_2 \parallel [10\bar{1}], \quad \mathbf{S}_3 \parallel [0\bar{1}\bar{1}]$$

in $SrCuTe_2O_6$ [Fig. 8(b)] to

$$\mathbf{S}_1 \parallel [1\bar{1}0], \quad \mathbf{S}_2 \parallel [\bar{1}01], \quad \mathbf{S}_3 \parallel [01\bar{1}]$$

would result in $E_2 = -\frac{3}{2}J_2S^2$ and allow the energy gain from AFM J_2 . This will lead to a different magnetic

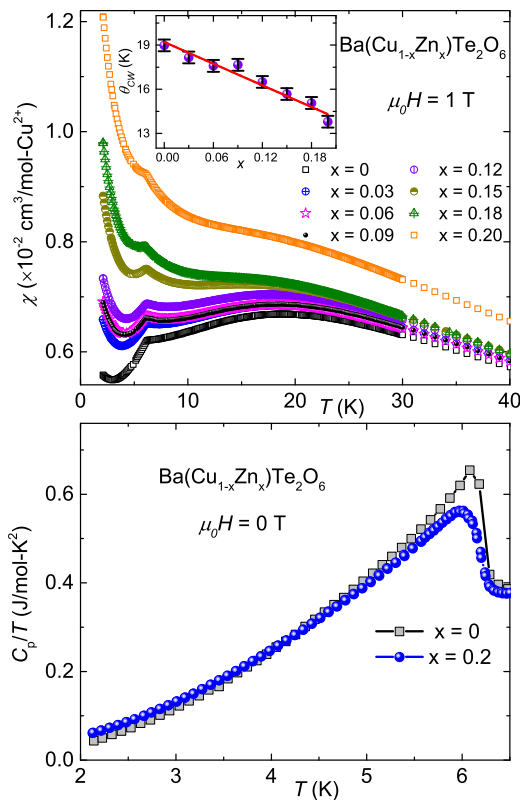


FIG. 11. Upper panel: $\chi(T)$ of $\text{Ba}(\text{Cu}_{1-x}\text{Zn}_x)\text{Te}_2\text{O}_6$ samples measured at $H = 1 \text{ T}$. Inset: Curie-Weiss temperature θ_{CW} as a function of doping concentration x with the solid line representing the linear fit. Lower panel: C_p/T of two end samples ($x = 0$ and 0.2) measured in zero magnetic field.

symmetry. It would be interesting to test this prediction experimentally if neutron data of the quality sufficient to discriminate between different magnetic symmetries could be obtained for $\text{BaCuTe}_2\text{O}_6$.

E. Magnetic dilution

Zn substitution can have two-fold effect on the magnetism of $\text{BaCuTe}_2\text{O}_6$. The change in the cubic lattice parameter tunes chemical pressure, whereas the introduction of non-magnetic Zn^{2+} ions dilutes the spin lattice. Figure 3 shows that changes in the lattice parameter are minimal, so the dilution effect should prevail. In the upper panel of Fig. 11, $\chi(T)$ of Zn-doped samples is plotted after normalizing to one mole of Cu^{2+} spins. Clearly, $\chi(T)$ at low temperatures increases systematically with increasing x . In spin systems, when non-magnetic Zn^{2+} is doped at the magnetic Cu^{2+} site, free Cu^{2+} ions are produced and cause the low-temperature paramagnetic upturn in $\chi(T)$. Additionally, magnetic dilution may create finite segments of spin chains that will also give rise to the Curie-like behavior [40]. Thus, our experimental

observations are consistent with the expected dilution effect.

The $\chi(T)$ data at high temperatures (above 200 K) were fitted by the CW law, Eq. (2). The value of C was found to vary between ~ 0.41 and $\sim 0.43 \text{ cm}^3\text{K}/\text{mol-Cu}^{2+}$, which corresponds to the effective moment $\mu_{\text{eff}} \simeq 1.81 - 1.85 \mu_B$. The obtained value of θ_{CW} is plotted as a function x in the inset of Fig. 11. As the doping level increases, θ_{CW} is found to decrease almost linearly from $\sim 19 \text{ K}$ ($x = 0$) to $\sim 14 \text{ K}$ ($x = 0.2$). This behavior is expected when some of the superexchange pathways are broken by the dilution, and the overall interaction energy gauged by θ_{CW} decreases [22].

Néel temperature should also be reduced by the dilution until long-range magnetic order disappears completely upon crossing the percolation threshold. The rate of this reduction and the value of the percolation threshold depend on the dimensionality of magnetic interactions and can be diagnostic for the interaction topology. For example, linear decrease in the T_N is expected for quasi-2D antiferromagnets [41], whereas superlinear decrease indicates further reduction in the dimensionality toward 1D [42] or an additional magnetic frustration in 2D [43]. Interestingly, $\text{BaCuTe}_2\text{O}_6$ follows neither of these scenarios. Its Néel temperature is remarkably insensitive to the dilution. Both the kink in $\chi(T)$ and the λ -type anomaly in $C_p(T)$ remain around 6.1 K even at $x = 0.2$ (Fig. 11). To our knowledge, it is the only example of a Cu^{2+} -based system, where long-range magnetic order is essentially unaffected by the Zn^{2+} substitution. One may understand this effect as a consequence of magnetic frustration for the interchain couplings, as discussed in Sec. III D. Dilution may alleviate the frustration of interchain couplings and keep T_N around the same value even though the overall energy of magnetic interactions is decreased.

IV. CONCLUSIONS

We have studied the effect of negative pressure on the frustrated network of the ACuTe_2O_6 compounds. Despite a significant increase in the cubic lattice parameter and individual Cu-Cu distances, the newly prepared $\text{BaCuTe}_2\text{O}_6$ strongly resembles its Sr sibling and shows a similar quasi-1D magnetic behavior driven by the dominant third-neighbor couplings J_3 forming spin chains. A closer examination of individual magnetic couplings revealed that the stretching of superexchange pathways caused by negative pressure not only reduces J_3 , but also increases AFM contribution to the second-neighbor coupling J_2 and likely changes its sign. This modification of the interchain coupling may be the cause of the subtle differences between the Sr and Ba compounds: the latter lacks the second phase transition at $T_{\text{N}2}$ as well as the field-induced transition around 3 T, but reveals minute spin canting.

We have also shown that the combination of frustrated

TABLE III. Atomic coordinates and atomic displacement parameters (U_{iso} , in units of 10^{-2} \AA^2) for $\text{SrCuTe}_2\text{O}_6$ at 80 K. The lattice parameter is $a = 12.4406(1) \text{ \AA}$, and the space group is $P4_132$.

Atom	Site	x/a	y/b	z/c	U_{iso}
Sr1	8c	0.05417(4)	0.05417(4)	0.05417(4)	0.43(2)
Sr2	4b	0.375	0.625	0.125	0.59(3)
Cu	12d	0.47634(7)	0.875	0.27366(7)	0.48(3)
Te	24e	0.33846(3)	0.91916(3)	0.05901(3)	0.35(1)
O1	24e	0.3722(3)	0.8200(3)	0.1713(3)	0.19(9)
O2	24e	0.2670(3)	0.8116(3)	-0.0227(3)	0.33(9)
O3	24e	0.2202(3)	0.9769(3)	0.1302(3)	0.91(9)

interchain couplings J_2 and J_6 may stabilize the non-collinear magnetic structure observed experimentally in $\text{SrCuTe}_2\text{O}_6$ [11, 12]. This scenario allows a generalized description of the Sr and Ba compounds in terms of a $J_2 - J_3 - J_6$ magnetic model, with the nearest-neighbor coupling J_1 systematically absent in both compounds due to its highly unfavorable superexchange geometry. The 3D spin-liquid behavior of $\text{PbCuTe}_2\text{O}_6$ requires the increase in AFM J_2 with the simultaneous reduction in J_3 and re-activation of J_1 [9]. The structural origin of these rather striking changes would be an interesting direction for future studies.

Note added: After completing this work, we became aware of an independent study of $\text{BaCuTe}_2\text{O}_6$ [44, 45]. Neutron diffraction experiments confirm different magnetic symmetries of $\text{SrCuTe}_2\text{O}_6$ and $\text{BaCuTe}_2\text{O}_6$, in agreement with our conclusion on the different sign of J_2 in these compounds.

ACKNOWLEDGMENTS

PB, NA, VS, and RN acknowledge SERB, India for financial support bearing sanction order no. CRG/2019/000960. The work in Augsburg was supported by the German Research Foundation (DFG) via the Project No. 107745057 (TRR80).

Appendix A: Crystallographic data for $\text{SrCuTe}_2\text{O}_6$

Here, in Table III, we present structural parameters for $\text{SrCuTe}_2\text{O}_6$ determined at 80 K using the same experimental setup as in the case of $\text{BaCuTe}_2\text{O}_6$ (Sec. II). The powder sample of the Sr compound from Ref. [10] was used for the synchrotron XRD measurement. The results are only marginally different from the previous reports [11, 12, 14], and facilitate a direct comparison between the two compounds.

-
- [1] L. Savary and L. Balents, Quantum spin liquids: a review, *Rep. Prog. Phys.* **80**, 016502 (2017).
- [2] J. Knolle and R. Moessner, A field guide to spin liquids, *Ann. Rev. Condens. Matter Phys.* **10**, 451 (2019).
- [3] C. Broholm, R. J. Cava, S. A. Kivelson, D. G. Nocera, M. R. Norman, and T. Senthil, Quantum spin liquids, *Science* **367**, eaay0668 (2020).
- [4] P. Mendels and F. Bert, Quantum kagome frustrated antiferromagnets: One route to quantum spin liquids, *C. R. Phys.* **17**, 455 (2016).
- [5] M. R. Norman, Colloquium: Herbertsmithite and the search for the quantum spin liquid, *Rev. Mod. Phys.* **88**, 041002 (2016).
- [6] D. S. Inosov, Quantum magnetism in minerals, *Adv. Phys.* **67**, 149 (2018).
- [7] B. Koteswararao, R. Kumar, P. Khuntia, S. Bhowal, S. K. Panda, M. R. Rahman, A. V. Mahajan, I. Dasgupta, M. Baenitz, K. H. Kim, and F. C. Chou, Magnetic properties and heat capacity of the three-dimensional frustrated $S = \frac{1}{2}$ antiferromagnet $\text{PbCuTe}_2\text{O}_6$, *Phys. Rev. B* **90**, 035141 (2014).
- [8] P. Khuntia, F. Bert, P. Mendels, B. Koteswararao, A. V. Mahajan, M. Baenitz, F. C. Chou, C. Baines, A. Amato, and Y. Furukawa, Spin liquid state in the 3D frustrated antiferromagnet $\text{PbCuTe}_2\text{O}_6$: NMR and muon spin relaxation studies, *Phys. Rev. Lett.* **116**, 107203 (2016).
- [9] S. Chillal, Y. Iqbal, H. O. Jeschke, J. A. Rodriguez-Rivera, R. Bewley, P. Manuel, D. Khalyavin, P. Steffens, R. Thomale, A. T. M. Nazmul Islam, J. Reuther, and B. Lake, Evidence for a three-dimensional quantum spin liquid in $\text{PbCuTe}_2\text{O}_6$, *Nature Comm.* **11**, 2348 (2020).
- [10] N. Ahmed, A. A. Tsirlin, and R. Nath, Multiple magnetic transitions in the spin- $\frac{1}{2}$ chain antiferromagnet $\text{SrCuTe}_2\text{O}_6$, *Phys. Rev. B* **91**, 214413 (2015).
- [11] P. Saeaan, Y. Zhao, P. Piyawongwatthana, T. J. Sato, F. C. Chou, M. Avdeev, G. Gitgeatpong, and K. Matan, Magnetic properties and magnetic structure of the frustrated quasi-one-dimensional antiferromagnet $\text{SrCuTe}_2\text{O}_6$, *Phys. Rev. B* **102**, 134407 (2020).
- [12] S. Chillal, A. T. M. N. Islam, H. Luetkens, E. Canévet, Y. Skourski, D. Khalyavin, and B. Lake, Magnetic structure of the quantum magnet $\text{SrCuTe}_2\text{O}_6$, *Phys. Rev. B* **102**, 224424 (2020).
- [13] B. Koteswararao, S. K. Panda, R. Kumar, K. Yoo, A. V. Mahajan, I. Dasgupta, B. H. Chen, K. H. Kim, and F. C. Chou, Observation of $S = 1/2$ quasi-1D magnetic and magneto-dielectric behavior in a cubic $\text{SrCuTe}_2\text{O}_6$, *J. Phys.: Condens. Matter* **27**, 426001 (2015).
- [14] L. Wulff and H. Müller-Buschbaum, Planare CuO_4 -Polygone und eine einseitig offene Te^{4+}O_3 -Koordination in $\text{SrCuTe}_2\text{O}_6$, *Z. Naturforsch. B* **52**, 1341 (1997).
- [15] K. Momma and F. Izumi, *VESTA 3* for three-dimensional visualization of crystal, volumetric and morphology data, *J. Appl. Crystallogr.* **44**, 1272 (2011).
- [16] J. Rodríguez-Carvajal, Recent advances in magnetic structure determination by neutron powder diffraction, *Phys. B: Cond. Matt.* **192**, 55 (1993).

- [17] V. Petříček, M. Dušek, and L. Palatinus, Crystallographic computing system jana2006: general features, *Z. Kristallogr. Cryst. Mater.* **229**, 345 (2014).
- [18] K. Koepnick and H. Eschrig, Full-potential nonorthogonal local-orbital minimum-basis band-structure scheme, *Phys. Rev. B* **59**, 1743 (1999).
- [19] J. P. Perdew, K. Burke, and M. Ernzerhof, Generalized gradient approximation made simple, *Phys. Rev. Lett.* **77**, 3865 (1996).
- [20] V. V. Mazurenko, M. V. Valentyuk, R. Stern, and A. A. Tsirlin, Nonfrustrated interlayer order and its relevance to the Bose-Einstein condensation of magnons in $\text{BaCuSi}_2\text{O}_6$, *Phys. Rev. Lett.* **112**, 107202 (2014).
- [21] R. Nath, K. M. Ranjith, J. Sichelschmidt, M. Baenitz, Y. Skourski, F. Alet, I. Rousochatzakis, and A. A. Tsirlin, Hindered magnetic order from mixed dimensionalities in CuP_2O_6 , *Phys. Rev. B* **89**, 014407 (2014).
- [22] K. M. Ranjith, M. Majumder, M. Baenitz, A. A. Tsirlin, and R. Nath, Frustrated three-dimensional antiferromagnet $\text{Li}_2\text{CuW}_2\text{O}_8$: ^7Li NMR and the effect of nonmagnetic dilution, *Phys. Rev. B* **92**, 024422 (2015).
- [23] D. C. Johnston, R. K. Kremer, M. Troyer, X. Wang, A. Klümper, S. L. Bud'ko, A. F. Panchula, and P. C. Canfield, Thermodynamics of spin $S = 1/2$ antiferromagnetic uniform and alternating-exchange Heisenberg chains, *Phys. Rev. B* **61**, 9558 (2000).
- [24] J. C. Bonner and M. E. Fisher, Linear magnetic chains with anisotropic coupling, *Phys. Rev.* **135**, A640 (1964).
- [25] S. Eggert, I. Affleck, and M. Takahashi, Susceptibility of the spin-1/2 Heisenberg antiferromagnetic chain, *Phys. Rev. Lett.* **73**, 332 (1994).
- [26] O. Janson, A. A. Tsirlin, J. Sichelschmidt, Y. Skourski, F. Weickert, and H. Rosner, Long-range superexchange in $\text{Cu}_2\text{A}_2\text{O}_7$ ($A = \text{P}, \text{As}, \text{V}$) as a key element of the microscopic magnetic model, *Phys. Rev. B* **83**, 094435 (2011).
- [27] P. W. Selwood, *Magnetochemistry*, 2nd ed. (Wiley-Interscience, New York, 1956) p. p. 78.
- [28] N. Motoyama, H. Eisaki, and S. Uchida, Magnetic susceptibility of ideal spin-1/2 Heisenberg antiferromagnetic chain systems, Sr_2CuO_3 and SrCuO_2 , *Phys. Rev. Lett.* **76**, 3212 (1996).
- [29] R. Nath, A. V. Mahajan, N. Büttgen, C. Kegler, A. Loidl, and J. Bobroff, Study of one-dimensional nature of $S = 1/2$ $(\text{Sr}, \text{Ba})_2\text{Cu}(\text{PO}_4)_2$ and BaCuP_2O_7 via ^{31}P NMR, *Phys. Rev. B* **71**, 174436 (2005).
- [30] B. Koteswararao, R. Kumar, J. Chakraborty, B.-G. Jeon, A. V. Mahajan, I. Dasgupta, K. H. Kim, and F. C. Chou, $\text{PbCu}_3\text{TeO}_7$: an staircase kagome lattice with significant intra-plane and inter-plane couplings, *J. Phys.: Condens. Matter* **25**, 336003 (2013).
- [31] E. S. R. Gopal, *Specific Heats at Low Temperatures* (Plenum, New York, 1966).
- [32] C. Kittel, *Introduction to Solid State Physics*, 8th ed. (Wiley, Hoboken, NJ, 2005).
- [33] Note that the values reported in this manuscript for $\text{SrCuTe}_2\text{O}_6$ may be slightly different from those in Ref. [10], because different structural parameters have been used.
- [34] S. Lebernegg, A. A. Tsirlin, O. Janson, and H. Rosner, Spin gap in malachite $\text{Cu}_2(\text{OH})_2\text{CO}_3$ and its evolution under pressure, *Phys. Rev. B* **88**, 224406 (2013).
- [35] H. J. Xiang, E. J. Kan, S.-H. Wei, M.-H. Whangbo, and X. G. Gong, Predicting the spin-lattice order of frustrated systems from first principles, *Phys. Rev. B* **84**, 224429 (2011).
- [36] A. A. Tsirlin, Spin-chain magnetism and uniform Dzyaloshinsky-Moriya anisotropy in BaV_3O_8 , *Phys. Rev. B* **89**, 014405 (2014).
- [37] S. Lebernegg, A. A. Tsirlin, O. Janson, R. Nath, J. Sichelschmidt, Y. Skourski, G. Amthauer, and H. Rosner, Magnetic model for $A_2\text{CuP}_2\text{O}_7$ ($A = \text{Na}, \text{Li}$): One-dimensional versus two-dimensional behavior, *Phys. Rev. B* **84**, 174436 (2011).
- [38] D. O. Nekrasova, A. A. Tsirlin, M. Colmont, O. Siidra, H. Vezin, and O. Mentré, Magnetic hexamers interacting in layers in the $(\text{Na}, \text{K})_2\text{Cu}_3\text{O}(\text{SO}_4)_3$ minerals, *Phys. Rev. B* **102**, 184405 (2020).
- [39] D. I. Badrtdinov, V. V. Mazurenko, and A. A. Tsirlin, Origin of up-up-down-down magnetic order in Cu_2GeO_4 , *Phys. Rev. B* **100**, 214401 (2019).
- [40] S. Eggert and I. Affleck, Impurities in $S = 1/2$ Heisenberg antiferromagnetic chains: Consequences for neutron scattering and Knight shift, *Phys. Rev. Lett.* **75**, 934 (1995).
- [41] A. L. Chernyshev, Y. C. Chen, and A. H. Castro Neto, Long-range order and low-energy spectrum of diluted 2D quantum antiferromagnet, *Phys. Rev. Lett.* **87**, 067209 (2001).
- [42] S. Eggert, I. Affleck, and M. D. P. Horton, Néel order in doped quasi-one-dimensional antiferromagnets, *Phys. Rev. Lett.* **89**, 047202 (2002).
- [43] P. Carretta, G. Prando, S. Sanna, R. De Renzi, C. Decorse, and P. Berthet, Evidence for impurity-induced frustration in La_2CuO_4 , *Phys. Rev. B* **83**, 180411(R) (2011).
- [44] A. Samartzis, *Magnetic investigation of effective spin-1/2 magnetic insulators based on 3d and 4f magnetic ions*, *Doctoral thesis*, Technische Universität Berlin, Berlin (2020).
- [45] A. Samartzis, D. Khalyavin, A. T. M. N. Islam, S. Chillal, K. Siemensmeyer, K. Prokes, D. J. Voneshen, A. Senyshyn, and B. Lake, Structural and magnetic properties of the new quantum magnet $\text{BaCuTe}_2\text{O}_6$, [arXiv:2102.07490](https://arxiv.org/abs/2102.07490).